FURTHER EXPERIMENTAL INVESTIGATIONS ON THE FAILURE OF CLAMPED BEAMS UNDER IMPACT LOADS

JILIN YU† and NORMAN JONES‡

Impact Research Centre, Department of Mechanical Engineering, The University of Liverpool, P.O. Box 147, Liverpool L69 3BX, U.K.

Abstract—Experimental results on the deformation and failure of clamped beams, made from aluminium alloy or mild steel and struck by a mass, are reported in this paper. Complete engineering and true stress–strain curves at strain rates up to 140 s^{-1} are presented for the materials. In addition, the dependence of rupture strain on strain rate is explored. These results provide experimental information of value for further numerical and theoretical studies on the dynamic inelastic failure of structures.

NOTATION

e	engineering strain
e_0	zero gauge-length elongation
$\dot{e}$	engineering strain rate
l_1	distance of impact point to the nearest support
p	exponent in the Cowper–Symonds equation
s	engineering stress
t	time
A_0	original cross-sectional area of a tensile specimen
A_f	smallest final cross-sectional area of a tensile specimen
B	beam breadth
D	material constant in the Cowper–Symonds equation
D_0	original diameter of the reduced section of a tensile specimen
D_2	original diameter of the enlarged ends of a tensile specimen in Fig. 1
E	Young's modulus
H	beam thickness
L_0	original length of the reduced section of a tensile specimen
L_1	equivalent length of the elastic part of the tensile test system defined in Fig. 23
P	load in a tensile test
V	impact velocity
V_0	initial impact velocity
W	maximum transverse deflection of a beam specimen
W_1–W_4	maximum permanent transverse displacements calculated using eqn (60) in Liu and Jones (1988) with different flow stresses
W_I	displacement of the impact point, as defined in Fig. 16
W_L	displacement of the point on the lower surface underneath the impact point as defined in Fig. 16
W_S	depth of indentation at the impact point
ε	true strain
$\dot{\varepsilon}$	true strain rate
θ	overall rotation angle at impact point defined in Yu and Jones (1989)
θ_c	critical overall rotation angle at fracture
σ	true stress
σ_y	yield stress; 0.2% proof stress for aluminium alloy and the lower yield stress for mild steel

Subscripts

f	value at fracture
m	value at the maximum load in a tensile test
p	permanent value

† Associate Professor, on leave from the University of Science and Technology of China, Hefei, Anhui, China. Visiting Royal Fellow.
‡ Professor of Mechanical Engineering and Head of Department.

1. INTRODUCTION

The behaviour of structures which are subjected to dynamic loads producing large inelastic strains is important for a broad class of engineering problems. An extensive literature on theoretical and experimental studies in this particular field is now available (Symonds, 1967; Johnson, 1972; Jones, 1989a,b,c; Reid, 1985). A rigid, perfectly plastic or elastic, perfectly plastic idealization of a material having an unlimited ductility is used frequently to simplify theoretical analyses. However, practical structures have a limited ductility and only a few experimental or theoretical studies have been published on the dynamic, inelastic failure of structures, as noted by Jones (1989d) and Duffey (1989).

An early experimental study on the dynamic, inelastic failure of beams was reported by Menkes and Opat (1973) and analysed using a simple rigid-plastic method by Jones (1976). More recently, a systematic study on the deformation and failure of fully clamped ductile beams struck by a mass has been conducted by Liu and Jones (1987a,b, 1988). Theoretical and numerical methods as well as experimental tests have examined both strain rate-insensitive and strain rate-sensitive materials. It is the object of these studies to develop failure criteria which may be used by designers in analytical or numerical methods. The results already gained emphasize the sensitivity of dynamic failure to the material properties. Future progress is possible by a partnership between experimental studies and numerical calculations, as discussed by Jones (1989e).

Unfortunately, there is not a sound understanding of the material properties under high rates of strain and large plastic strains, which are important for this class of practical problems. There is also a paucity of experimental data on the variation of rupture strain with strain rate, even for uniaxial behaviour (Kawata et al., 1968; Harding, 1977; Soroushian and Choi, 1987; Al-Mousawi et al., 1987). Moreover, only the elongation to fracture, i.e., an ultimate engineering strain, which depends on the gauge length when necking takes place, is usually recorded in these tests.

This paper is a continuation of the previous studies reported by Liu and Jones (1987a,b, 1988), and Yu and Jones (1989). A series of uniaxial tensile tests on aluminium alloy and mild steel specimens have been conducted in order to provide adequate data on the material properties at various strain rates and large strains for theoretical methods and numerical codes. In particular, the variation of the true rupture strain with strain rate is examined. More experimental tests on the deformation and failure of clamped beams struck by a mass are reported with detailed information for further investigations.

The tensile tests cover a strain rate range from 10^{-3} s^{-1} to 140 s^{-1}. Complete engineering and true stress–strain curves have been obtained and the strain rate sensitivity of plastic flow for mild steel at large strains obeys the well-known Cowper–Symonds constitutive equation with appropriate constants.

The impact tests on fully clamped beams are similar to those reported earlier by Liu and Jones (1987a). However, emphasis is placed on the transverse shear failure of the aluminium alloy specimens struck near a support and on the influence of material strain rate sensitivity on the failure of the mild steel specimens. Although only a small number of specimens have been tested, an effort is made to obtain more comprehensive information from each test which is required for future theoretical and numerical studies.

2. TENSILE TESTS

2.1. Specimen preparation

Table 1 lists the chemical composition and Young's moduli of the aluminium alloy and mild steel examined in this paper. The tensile test specimens and fully clamped beams were cut from the same block of material. After machining, all the mild steel specimens were heated in a vacuum furnace at 920°C for 3 h and then allowed to cool to 650°C before being quenched with nitrogen gas.

2.2. Experimental technique

The quasi-static tensile tests ($\dot{e} < 2 \times 10^{-2}$ s^{-1}) were conducted on a standard DARTEC testing machine and the dynamic tests were carried out using a 50 kN ESH

Table 1. Chemical composition and Young's modulus of specimen materials

Material	Chemical composition (%)											E (GN m^{-2})
	C	Si	Mn	P	S	Cr	Ni	Al	Cu	Fe	Mg	
Mild steel	0.22	0.02	1.12	0.019	0.028	<0.02	0.03	<0.005	0.02			208
Aluminium alloy		0.12	0.75				0.12	0.01	0.04	0.27	4.27	73
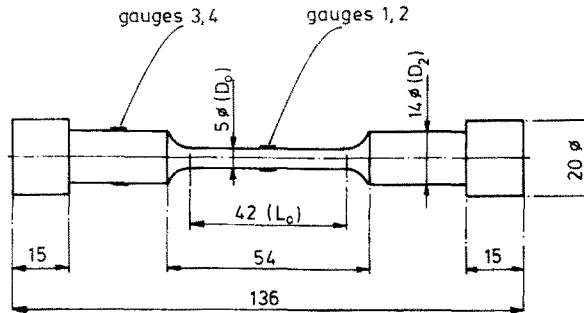
Fig. 1. Dynamic tensile test specimens. Gauges 1 and 2 measure the engineering strain, gauges 3 and 4 measure the axial load (dimensions in mm).

servo-hydraulic testing machine. A slack adaptor was fitted in the ESH machine which allowed the machine actuator to accelerate for a distance before the specimen was loaded. Thus, a constant velocity was achieved under closed-loop control. This arrangement gave a maximum strain rate of 140 s^{-1}, which is similar to that actually reached in some previous beam tests according to the numerical simulation reported by Yu and Jones (1989). The strain gauge bridge output was recorded during the dynamic tests using a DL 1080 transient recorder together with a Tektronix AM 502 differential amplifier. The load cell outputs and cross-head displacements were recorded directly by a DL 1080 transient recorder.

The nominal dimensions of the dynamic test specimens are shown in Fig. 1 and, to ensure comparability, the quasi-static test specimens have the same dimensions but without the enlarged ends.

The engineering stress is calculated from the load cell record. However, the load cell record exhibited a strong vibration for the tests at the highest strain rate due to stress wave propagation effects.† Hence an extra pair of strain gauges was adhered to the elastically deforming enlarged end of each specimen, as shown in Fig. 1. It was found from a static calibration that the axial load calculated from these two strain gauges was 2% lower than the actual value due to the triaxial state of stress in the specimens. This effect was taken into account in the data processing. Figure 2 shows a comparison between the data obtained from the strain gauges on the enlarged ends and the load cell record at a strain rate of $\dot{e} = 16.7$ s^{-1}. A negligible difference is found between the two curves except at the initial stage before the stress distribution in a specimen is uniform. At a strain rate of $\dot{e} = 140$ s^{-1}, the initial period of non-uniform strain is longer. Nevertheless, the experimental data are still reliable, at least for $t \geqslant 0.35$ ms or $e \geqslant 0.04$.‡

The engineering strain-time history was recorded by a pair of EP-08-125AD-120-type strain gauges located at the middle of a test specimen. These strain gauges are valid for engineering strains up to about 20%. The non-uniform deformation after necking leads to an engineering strain which depends on the gauge length. Here the stress-strain curve after

---

† The load cell is located at the bottom of the machine and far from the test specimen.
‡ At the highest strain rate ($\dot{e} = 140$ s^{-1}), the time duration of a test is about 2 ms. This is about one order of magnitude longer than the time required for a plastic wave to travel along a specimen. The plastic wave speed in the initial stage is estimated as 600 m s^{-1}, approximately. Thus, the plastic stress wave travels five times the specimen length of 42 mm in the reduced section in approximately 0.35 ms, when the strain is about 0.04.
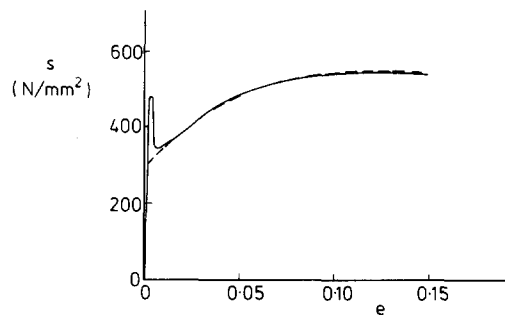
Fig. 2. Engineering stress–strain curves for mild steel specimen S13 at a strain rate of 16.7 s⁻¹.
(———) Based on strain gauges 3 and 4 in Fig. 1. (– – –) Based on load cell record.

necking is obtained using the cross-head displacement–time history, which is associated with a gauge length of 42 mm, within which plastic flow takes place. However, proper correction of the data is necessary in order to account for the limited stiffness of the testing machine as illustrated in Appendix A. Two engineering stress–strain curves which were obtained using strain gauges and the cross-head displacement method are compared in Fig. 3. The cross-head displacement method was also used when the strain gauges failed before the ultimate tensile stress was reached in a test.

Although the maximum engineering stress can be determined accurately, it is difficult to determine the corresponding time. Therefore, the associated strain e_m, i.e., the strain when the instability is initiated, cannot be determined accurately from the s–t and e–t curves. Thus, e_m was obtained after a test by measuring the diameter of the specimen which lies outside the necked region and using the assumption of plastic incompressibility. In other words, it is assumed that no further plastic deformation develops in that part once necking has commenced.

The true stress and strain before necking are obtained from the expressions

$$\sigma = s(1+e) \quad \text{and} \quad \varepsilon = \ln(1+e) \tag{1a,b}$$

respectively. Now, necking is a local phenomenon so that a zero gauge length must be used to calculate the true strain after necking. The zero gauge length elongation at fracture is obtained from the specimen diameter in the necked region, or

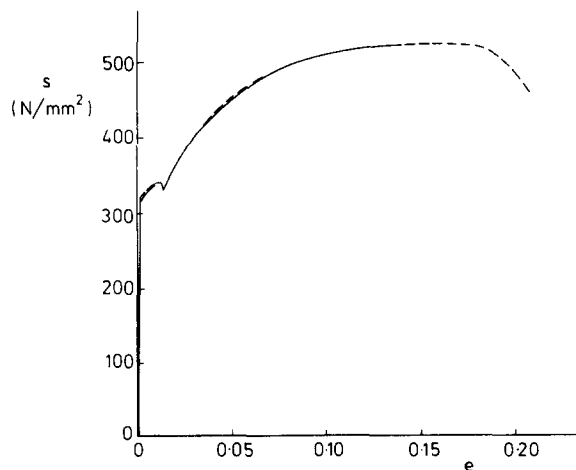$$e_0 = (A_0 - A_f)/A_f \quad \text{and} \quad \varepsilon_f = \ln(A_0/A_f), \tag{2a,b}$$

Fig. 3. Engineering stress–strain curves for mild steel specimen S15 at a strain rate of 0.53 s⁻¹.
(———) Strain measured by strain gauges. (– – –) Strain calculated from cross-head displacement.
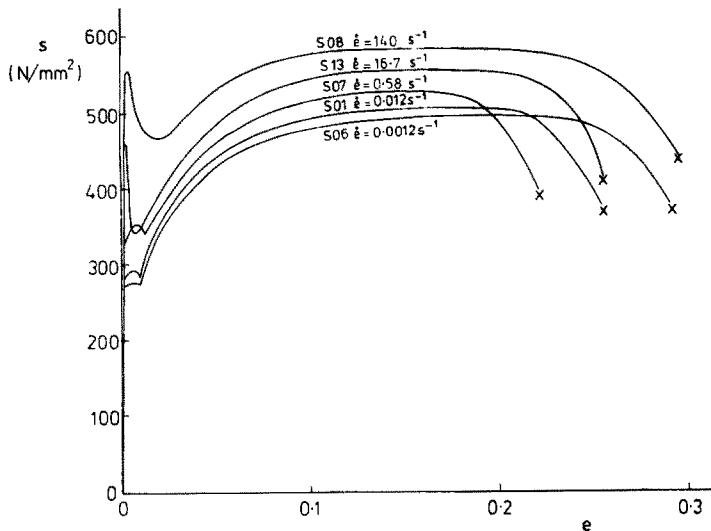
Fig. 4. Engineering stress–strain curves for mild steel specimens at different strain rates. The gauge
length is 42 mm.

while the fracture stress is

$$\sigma_f = P_f / A_f, \tag{2c}$$

where no correction is made to σ_f to compensate for the triaxial state of stress in the necked
region. Unfortunately, the specimen diameter–time history before fracture was not recorded
so that the curve between $(\varepsilon_m, \sigma_m)$ and $(\varepsilon_f, \sigma_f)$ is taken as a straight line, which is a normal
approach for quasi-static tests, e.g., see *Metals Handbook* (1985).

2.3. Results for the mild steel specimens

Five different strain rates were chosen for the mild steel specimens and two to five tests
were performed at each strain rate. The lower yield stress, the stresses and strains at the
onset of necking and at fracture are listed in Table 2.†

A set of engineering stress–strain curves is plotted in Fig. 4 for the five strain rates,
and the associated true stress–strain curves are shown in Fig. 5. The variation of the true
stresses at different true strains with the logarithm of the engineering strain rate is presented
in Fig. 6, while Fig. 7 shows the variation of the lower yield stress, ultimate stress and
rupture stress also with the logarithm of the engineering strain rate. These results indicate
that the material exhibits a rather consistent strain rate-sensitive behaviour at large strains
($\varepsilon \geqslant 0.05$), but that the lower yield stress, as well as the flow stress at small strains, is
significantly more strain rate-sensitive. This is in accordance with the results reported by
other investigators on structural steel, e.g., see Soroushian and Choi (1987) and Campbell
(1972).

The variation of the rupture strain with the logarithm of the engineering strain rate is
shown in Fig. 8. It is evident that a minimum engineering rupture strain occurs at a strain
rate of about $10\ \text{s}^{-1}$. A somewhat similar behaviour was observed by Harding (1977) for
four alloy steels though this phenomenon is not always recorded in experiments, as discussed
by Jones (1989f). It is interesting to note that the true rupture strain is about 0.83 and is
nearly independent of the strain rate for this material over the entire range from 10^{-3} to
$10^2\ \text{s}^{-1}$, though the true rupture stress increases about 20%.

The difference in the material strain rate sensitivity between the initial stage of plastic
flow and that at larger strains causes some difficulty in developing a consistent dynamic
constitutive relationship. However, it is possible to model the dynamic behaviour in the

---

† The engineering rupture strains listed in Table 2 were obtained by measuring the total elongation after a
test. These values are more reliable but may differ slightly from those obtained from the dynamic records.

Table 2. Experimental details of mild steel tensile specimens

| Specimen number	D_0 (mm)	D_2 (mm)	σ_y (N mm^{-2})	e_m	ε_m	s_m (N mm^{-2})	σ_m (N mm^{-2})	e_f	e_0	ε_f	s_f (N mm^{-2})	σ_f (N mm^{-2})	$\dot{e}$ (s^{-1})
S03	5.00		270	0.192	0.176	500	596	0.275	1.30	0.831	362	830	0.0012
S06	5.02		269	0.207	0.188	494	598	0.290	1.40	0.876	369	855	0.0012
S02	5.05		252	0.135	0.127	488	554	0.210	1.16	0.768	369	775	0.0012
S05	5.00		285	0.202	0.182	511	614	0.259	1.24	0.807	376	842	0.012
S01	5.03		275	0.201	0.182	503	604	0.250	1.32	0.843	367	854	0.012
S15	4.97	13.83	328	0.172	0.157	524	614	0.214	1.24	0.807	390	873	0.53
S07	5.03	14.02	336	0.126	0.119	525	591	0.217	1.35	0.855	387	910	0.68
S09	5.04	13.89	327	0.175	0.161	523	614	0.235	1.32	0.841	397	921	0.49
S14	5.03	13.78	358	0.145	0.135	559	640	0.211	1.28	0.825	408	931	16.7
S13	5.03	13.99	340	0.155	0.144	554	640	0.226	1.29	0.830	406	931	16.7
S08	4.93	14.01	460	0.182	0.167	580	685	0.256	1.25	0.813	434	978	140
S04	4.88	13.92	464	0.197	0.180	586	701	0.272	1.48	0.907	403	998	140
S10	5.01	13.86	420	0.176	0.162	590	694	0.254	1.41	0.878	407	980	128
S11	4.98	13.90	430	0.208	0.189	586	707	0.269	1.35	0.853	398	934	140
S12	5.04	14.02		0.175	0.161	576	677	0.246	1.39	0.871	408	975	140
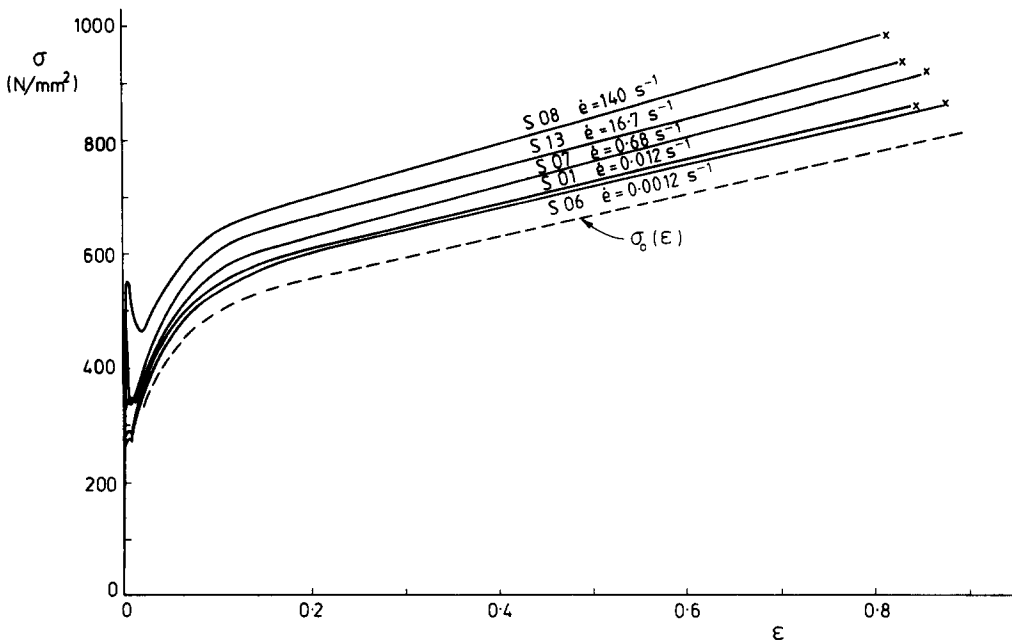
Fig. 5. True stress–strain curves for the mild steel specimens at different strain rates in Fig. 4. The fictitious static stress–strain curve $\sigma_0(\varepsilon)$ is used for fitting the Cowper–Symonds equation to the data.
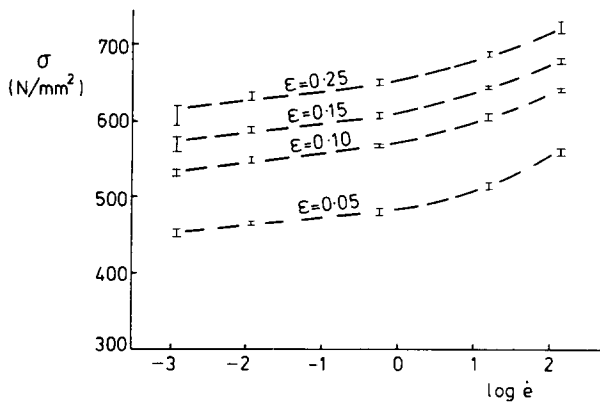

Fig. 6. Variation of the true stress with strain rate at different true strains for the mild steel specimens.

initial stage and at large plastic strains separately. The behaviour of large plastic strains would be relevant for a failure analysis.

Now, the well-known Cowper–Symonds empirical expression (Symonds, 1965), is

$$\sigma = \sigma_0(\varepsilon)[1 + (\dot{\varepsilon}/D)^{1/p}], \tag{3}$$

where $\sigma_0(\varepsilon)$ is the static stress–strain relation and D and p are constants which are chosen to described the strain rate-sensitive behaviour of a material. Equation (3) fits the present experimental results in the strain range from 0.04 up to rupture strain when

$$D = 1.05 \times 10^7 \, \text{s}^{-1} \quad \text{and} \quad p = 8.30, \tag{4}$$

together with a fictitious static stress–strain relation, which is shown by the dotted line in Fig. 5. The method of data fitting is described in Appendix B. These values of D and p are much larger than those reported by other investigators for steels. The difference arises mainly
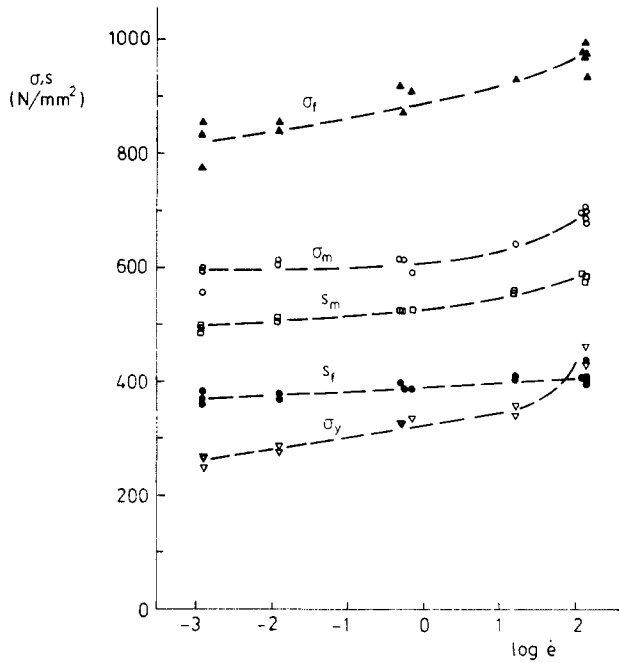
Fig. 7. Variation of the lower yield stress, ultimate tensile stress and rupture stress with strain rate
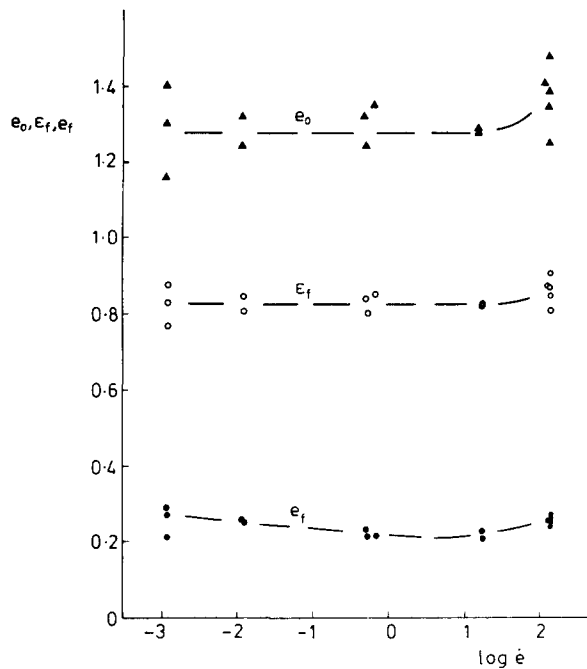for the mild steel specimens.

Fig. 8. Variation of the rupture strain with strain rate for the mild steel specimens.

from the use of true stress–strain curves for strains larger than $\varepsilon = 0.04$ and a fictitious
static stress–strain curve in order to obtain the best fit with the experimental data. Other
investigators have used the engineering stress–strain curves and employ a quasi-static stress–
strain curve for the static one.† As mentioned earlier, the values of ε_m and ε_f which were

† The values of D and p are sensitive to the $\sigma_0(\varepsilon)$ curve which is used in eqn (3). For example, $D = 1.84 \times 10^5$ s^{-1} and $p = 4.63$ if the data at $\dot{e} = 0.0012$ s^{-1} are used as $s_0(e)$ to fit the engineering stress–strain curve. However, $D = 6.4 \times 10^6$ s^{-1} and $p = 8.31$ when a fictitious static curve is used to obtain the best fit. Thus, it is difficult to make comparisons with other investigators who replace the static curves by quasi-static stress–strain curves which have been obtained at various strain rates.

used in the curve fitting were obtained from the reduction in area measured after the tests, and, therefore, are accurate.

2.4. *Results for the aluminium alloy specimens*

The tensile test results for the aluminium alloy specimens are given in Table 3 and shown in Figs 9–11 for three different strain rates. The shape of a cross-section after a
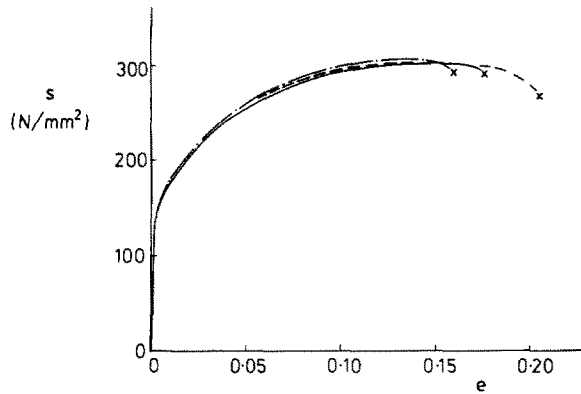

Fig. 9. Engineering stress–strain curves for the aluminium alloy specimens. (——) Specimen A01, $\dot{e} = 2.4 \times 10^{-3}$ s^{-1}. (—·—·—) Specimen A15, $\dot{e} = 1.2 \times 10^{-3}$ s^{-1}. (———) Specimen A09, $\dot{e} = 1.4 \times 10^{2}$ s^{-1}.
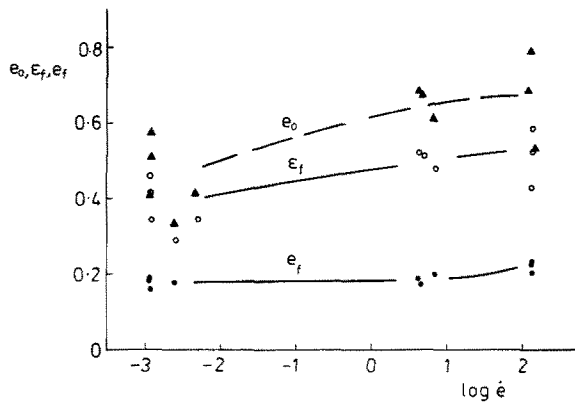

Fig. 10. Variation of the rupture strain with strain rate for the aluminium alloy specimens.
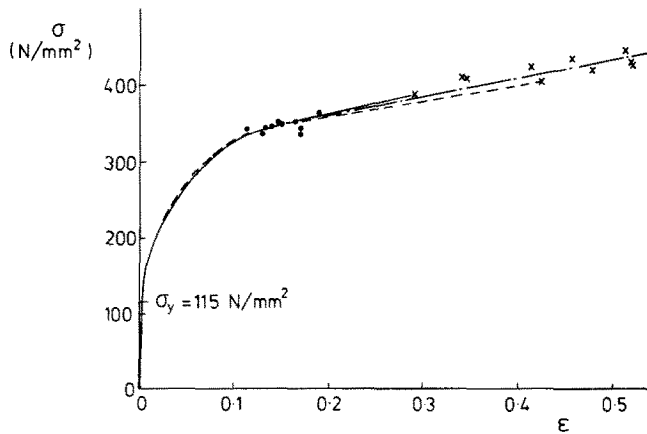

Fig. 11. True stress–strain curves for the aluminium alloy specimens A01 and A09, and the stresses and strains for the other aluminium alloy specimens at maximum load and at fracture. (——) Specimen A01, $\dot{e} = 2.4 \times 10^{-3}$ s^{-1}. (———) Specimen A09, $\dot{e} = 1.4 \times 10^{2}$ s^{-1}. (————) Proposed uniform σ–ε curve. (×) Rupture stress and strain. (●) Stress and strain at the maximum load.

Table 3. Experimental details of aluminium alloy tensile specimens

Specimen number	D_0 (mm)	D_2 (mm)	σ_y (N mm^{-2})	e_m	ε_m	s_m (N mm^{-2})	σ_m (N mm^{-2})	e_f	e_0	ε_f	s_f (N mm^{-2})	σ_f (N mm^{-2})	$\dot{e}$ (s^{-1})
A15	4.90			0.120	0.113	307	344	0.160	0.408	0.342	292	411	0.0012
A11	4.96			0.143	0.134	302	346	0.188	0.511	0.413	282	425	0.0012
A17	4.97			0.158	0.147	302	350	0.181	0.579	0.457	276	436	0.0012
A01	4.96		115	0.178	0.164	301	355	0.176	0.337	0.290	290	387	0.0024
A02	4.97		114	0.163	0.151	300	349		0.412	0.345	288	408	0.0048
A07	4.99			0.185	0.170	284	337	0.186	0.681	0.520	256	430	4.4
A14	4.95			0.138	0.130	296	337	0.171	0.670	0.513	266	444	4.9
A10	5.00			0.185	0.170	287	340	0.198	0.613	0.478	261	421	6.8
A09	5.02	13.99		0.151	0.140	302	347	0.205	0.529	0.425	266	407	140
A13	5.01	14.02		0.203	0.185			0.229	0.785	0.580			140
A08	4.97	13.96		0.210	0.190	301	364	0.226	0.683	0.520	253	426	130

tensile test was elliptic with ratios of the minor to major axes varying from 0.86 to about 1. This is attributed to the anisotropy and inhomogeneity of the specimen material and is possibly responsible for the scatter of the data, which is greater in comparison with the results for the steel specimens, especially after necking.

Two quasi-static engineering stress–strain curves and a dynamic one ($\dot{e} = 140 \text{ s}^{-1}$) are presented in Fig. 9. It is evident that strain rate does not influence the plastic flow before necking although the curves after the onset of instability are somewhat different. It transpires from Fig. 10 that both the engineering and true rupture strains increase with an increase in the strain rate. An increase in the fracture elongation was also reported by Kawata et al. (1968) for the experimental results on aluminium and aluminium alloy tensile specimens with strain rates having values up to those in the present study. However, it is evident from Fig. 11 that no significant difference is found in the plastic flow behaviour after necking. Figure 11 contains two true stress–strain curves (quasi-static and dynamic), as well as all the data points at fracture and at maximum load. It appears that all these data could be represented by the single curve shown in this figure, and that the strain rate affects only the rupture conditions.

3. BEAM TESTS

3.1. Experimental details

Impact tests were conducted on beams using the drop hammer rig shown in Fig. 12. The striking mass used in this study weighed 5 kg and the drop height may be adjusted to obtain the required impact velocity. The tup head was quench hardened and the impact area was 5.08 mm wide. The reader is referred to Liu and Jones (1987a) and Birch et al. (1988) for more details of the drop mass rig.

Flat specimens with a nominal cross-sectional area $B \times H = 10.16 \times 6.35 \text{ mm}^2$ were fully clamped across a span of 101.6 mm, as shown in Fig. 13.

Two impact positions were chosen for each material. One at the mid-span, i.e. $l_1 = 50.8$ mm, and the other at $l_1 = 25.4$ mm for the mild steel beams and at $l_1 = 6.35$ mm for the aluminium alloy beams. A few dynamic tests were conducted with varying impact velocities at each impact position until, in some cases, a specimen just broke. Typical engineering and true strain–time curves are shown in Fig. 14 for a strain gauge which was attached to the lower surface† immediately underneath the impact point. The impact velocity of the tup was measured using a laser Doppler velocimeter (LDV), which was then integrated to obtain the displacement of a specimen at the impact point, W_1. Typical velocity–time and displacement–time curves are shown in Fig. 15.

The deformation of a beam specimen was also recorded by a high speed camera at about 11,660 one-half frames per second, which gave a time resolution of about 86 μs. The film was analysed in order to obtain the deformation–time history of a specimen and the time and the maximum deflection at the onset of fracture when a specimen broke during a test.

If a specimen did not break during a test, then the maximum permanent transverse deflection W_p and the permanent transverse displacement of the point on the lower surface underneath the impact point, W_{Lp}, were measured using Vernier calipers before the specimen was released from the support clamps. The indentation depth at the impact point was also measured using Vernier calipers.

One quasi-static test was conducted until failure at each impact position using the same specimen holder and loading tup in a DARTEC standard testing machine. A strain gauge recorded the tensile strain on the lower surface underneath the load point and a digital Vernier height gauge was used to measure the transverse displacement at the same position.

It should be noted that the maximum deflection W, the displacement of the impact point W_1, and the displacement of the lower surface underneath the load point, W_L, are not identical, as illustrated in Fig. 16. They were measured by different methods and at different positions.

---

† The surface which is in contact with the striker is defined as the upper surface of a specimen.
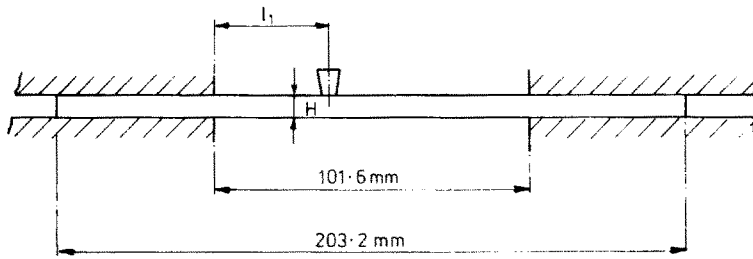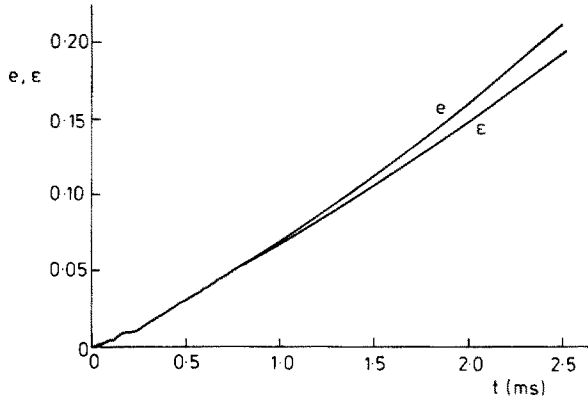
Fig. 13. Beam tests.

Fig. 14. Engineering and true strain–time histories for aluminium alloy beam specimen AB05 with $l_1 = 50.8$ mm and $V_0 = 6.2$ m s^{-1}.
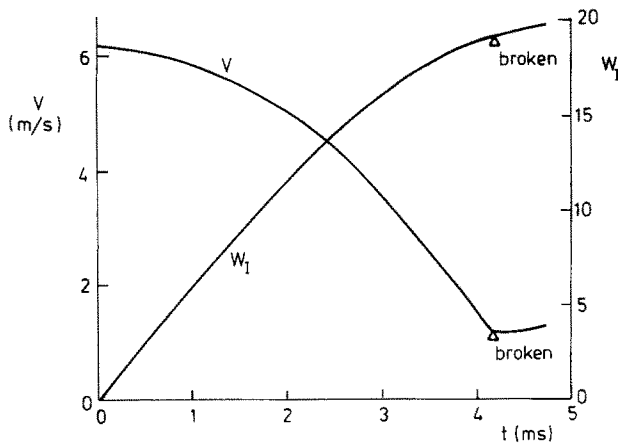

Fig. 15. Impact velocity–time history measured by the LDV and the corresponding displacement–time history for specimen AB05 with $l_1 = 50.8$ mm and $V_0 = 6.2$ m s^{-1}.
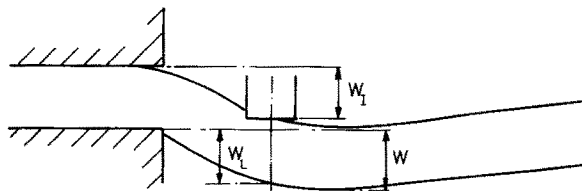

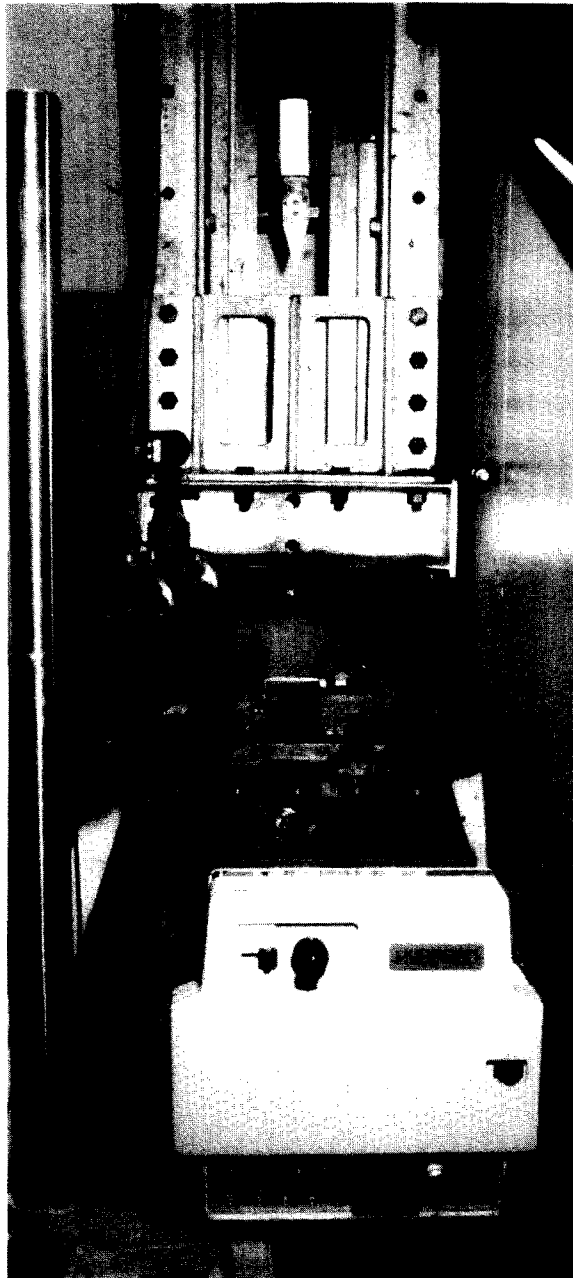Fig. 16. Definition of beam displacements W_1, W_L and W.

Fig. 12. Experimental set-up for the beam tests showing the drop hammer rig with the laser Doppler
velocimeter and high speed camera.

Table 4. Experimental details of mild steel beams

Specimen number	H (mm)	B (mm)	l_1 (mm)	V_0 (m s^{-1})	W_p (mm)	W_{Lp} (mm)	W_f (mm)	W_s (mm)	Comments
SB10	6.29	10.21	50.8				20.1		quasi-static test
SB09	6.29	10.10	50.5	10.5	20.90	20.90		0.5	
SB08	6.20	10.13	49.9	10.6			21.8		just broken
SB06	6.20	10.16	50.8	11.5			22.8		broken
SB03	6.19	10.22	25.4+0.4†				$W_{Lf} = 16.46$		quasi-static test
SB07	6.20	10.17	25.4	8.8	14.52	13.90		1.1	crack and severe necking
SB05	6.23	10.06	25.4	9.2			15.0		broken
SB04	6.30	10.18	25.4	10.1			16.0		broken

† Load position moved. 0.4 mm towards the mid-span during the response.

Table 5. Experimental details of aluminium alloy beams

Specimen number	H (mm)	B (mm)	l_1 (mm)	V_0 (m s^{-1})	W_p (mm)	W_{Lp} (mm)	W_f (mm)	W_s (mm)	Comments
AB02	6.38	10.24	50.8				16.5		quasi-static test
AB04	6.36	10.23	50.8	5.4	14.80	14.80		0.2	
AB10	6.39	10.19	50.8	5.8	15.90	15.90		0.3	
AB05	6.41	10.22	50.8	6.2			17.7		just broken
AB03	6.40	10.21	6.35				$W_{Lf} = 3.34$		quasi-static test
AB08	6.40	10.23	6.35	3.7	3.84	3.22		0.7	
AB09	6.39	10.20	6.35	3.8	4.18	3.60		0.9	severe indentation

3.2. Results

The experimental details for the mild steel and aluminium alloy beams are listed in Tables 4 and 5, respectively.

It is evident from the transverse load versus transverse deflection relationships for quasi-static loads in Fig. 17a–d that there are no significant differences for specimens loaded
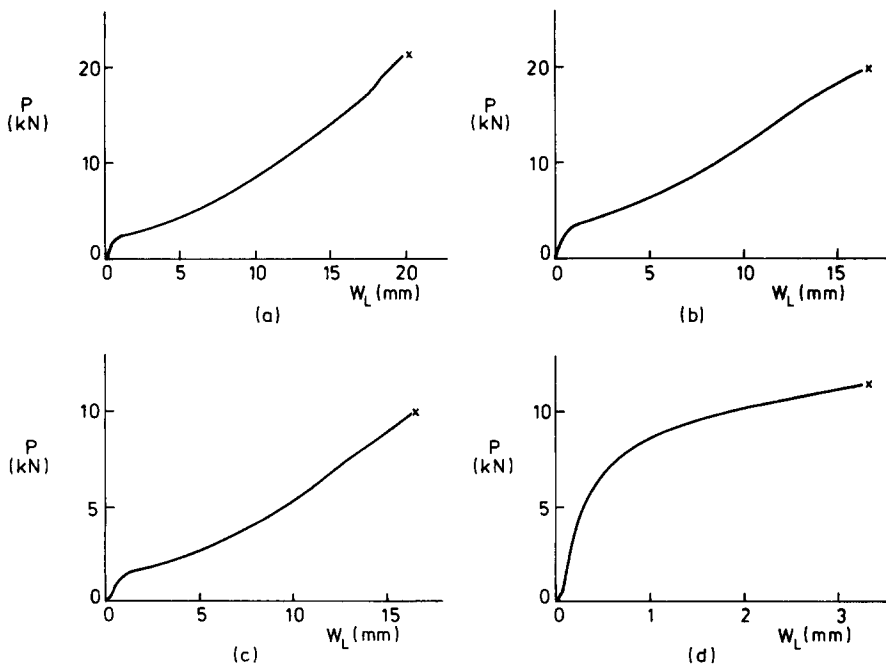

Fig. 17. Quasi-static load–displacement curves for the beams. (a) SB10, $l_1 = 50.8$ mm. (b) SB03, $l_1 = 25.4+0.4$ mm (see footnote to Table 4). (c) AB02, $l_1 = 50.8$ mm. (d) AB03, $l_1 = 6.35$ mm.
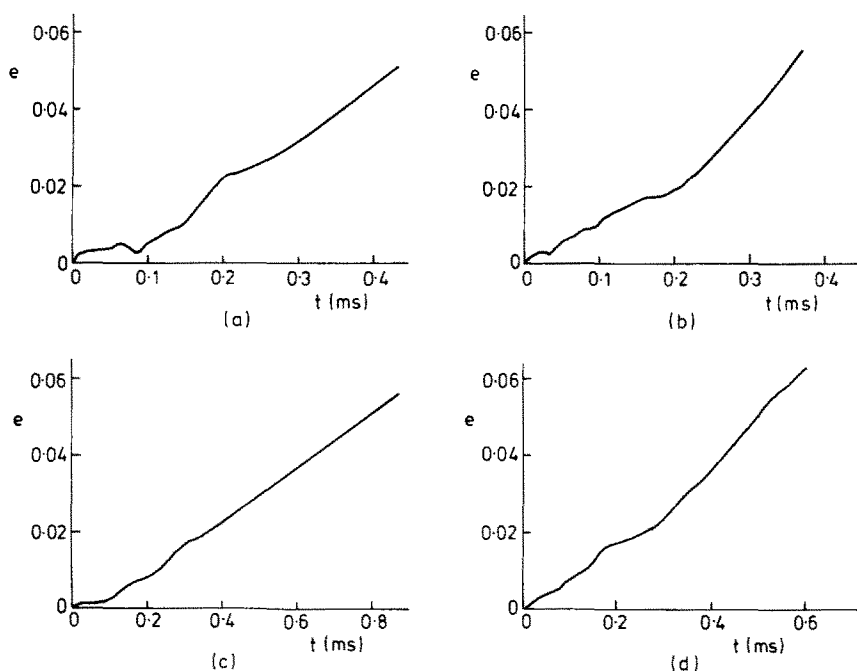
Fig. 18. Engineering strain–time histories during the early stage of motion for (a) SB08, $l_1 = 49.9$ mm, $V_0 = 10.6$ m s^{-1}; (b) SB05, $l_1 = 25.4$ mm, $V_0 = 9.2$ m s^{-1}; (c) AB10, $l_1 = 50.8$ mm, $V_0 = 5.8$ m s^{-1}; (d) AB09, $l_1 = 6.35$ mm, $V_0 = 3.8$ m s^{-1}.

at the mid-span or at the quarter-span. However, the character of the response is different for the aluminium alloy specimen loaded near a support.

It was found in the dynamic tests that the tensile strain on the lower surface underneath the impact point increases almost linearly with time except for very early times. A strain rate of about 80 s^{-1} is estimated† from the true strain–time history of the aluminium alloy beam specimen AB05 shown in Fig. 14. The maximum strain rate is somewhat larger because the strain gauge has a finite gauge length (3.175 mm). The strain–time histories in the initial stage, however, are quite different and depend on the specimen material and the impact position. When a beam is impacted at a point near a support, the strain in the initial stage increases monotonically and consistently, as shown in Figure 18d. However, when it is impacted at its mid-span, the strain in the initial stage increases slowly. It is observed for both steel and aluminium alloy specimens that the strain remains nearly constant for a short time interval, as shown in Fig. 18a,c. In addition, a drop in the strain after this interval was detected for the steel specimens, as shown in Fig. 18a,b. This phenomenon is possibly related to the instability of the steel when plastic yielding occurs.

It is evident from Fig. 16 that the indentation may be obtained approximately from the difference between the W_L–t and W_I–t curves. Unfortunately, it is difficult to measure the W_L–time history when a beam is impacted unsymmetrically. However, W is only slightly larger than W_L when the impact point is not near a support, and hence the W–t curve may be used for a qualitative analysis.

The W_I–t and W–t curves obtained from the LDV records and the high speed film for specimen SB07 are plotted in Fig. 19. An analysis of the film gives a maximum permanent transverse deflection W_p of 14.40 mm, which is in good agreement with 14.52 mm measured after the test. Figure 19 reveals that both W_I and W reach the peak values at $t = 3$ ms, but with W_I about 0.9 mm larger than W. This is in reasonable agreement with an indentation of 1.1 mm which was measured at the impact point. It transpires that the indentation occurs mainly during the second half of the loading process for specimens which are loaded at or

† No distinction is made in this paper between engineering strain rate and true strain rate because of the negligible differences.
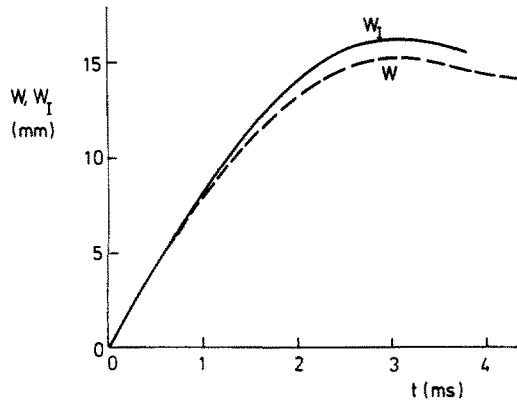
Fig. 19. Comparison of the W_I–t curve from the LDV record with the W–t curve from the high speed film for specimen SB07 with $l_1 = 25.4$ mm and $V_0 = 8.8$ m s^{-1}.

near the mid-span. This is in accordance with the load–deflection curves for the quasi-static tests because the load becomes large only for large displacements, as shown in Fig. 17a–c. On the other hand, it is expected that the indentation would occur earlier when a beam is impacted near a support, since the load rises rapidly with deflection, as shown in Fig. 17d.

The strain–displacement curves from the dynamic and quasi-static tests are compared in Fig. 20a–d. These curves are almost coincident for the aluminium alloy beams struck at the mid-span, as shown in Fig. 20c, with a difference of less than 5% for large deformations and strains. It was also shown for the numerical results reported in Fig. 13 of Yu and Jones (1989) that a common maximum tensile strain–maximum transverse displacement curve was obtained regardless of the impact velocity for a given beam. It is evident from Fig. 20c that the strain distribution is almost independent of the type of loading and so the influence of inertia is negligible.† However, the difference between the curves is larger when an aluminium alloy beam is impacted near a support, as indicated in Fig. 20d.

The dynamic strain–displacement curves for the mild steel beams are smaller than the quasi-static ones at small deflections, and are larger for large deflections, as shown in Fig. 20a,b. It transpires that the strain distributions in the dynamically loaded mild steel beams, which are strain rate-sensitive, are different from those in the corresponding quasi-static tests. This is not surprising because the strain rate at different parts of a dynamically loaded beam is different and, thus, the level of strain hardening is different, i.e. different parts of a beam have different stress–strain relations. The specimen behaves as if it was made from a material having a non-homogeneous strength. Moreover, the strain distribution in the initial stage may be affected by the influence of stress wave propagation and the material yield instability.

An approximate rigid, perfectly plastic analysis, which retains the influence of finite-deflections or geometry changes, was reported in Section 4 of Liu and Jones (1988) for the present problem. The maximum permanent transverse displacement is predicted by eqn (60) in Liu and Jones (1988) and requires the plastic flow stress, which is difficult to select in the present study because of the important influence of strain hardening and the significant effects of material strain rate sensitivity for the mild steel beams.

The maximum permanent transverse displacements W_1 and W_2 in Table 6 were obtained from eqn (60) in Liu and Jones (1988) for the aluminium alloy beams with a flow stress equal to the yield stress ($\sigma_y = 115$ N mm^{-2}) and the ultimate tensile stress ($s_m = 300$ N mm^{-2}), respectively. Similarly, the maximum permanent transverse displacements W_1–W_4 in Table 7 were calculated using σ_y and s_m at $\dot{e} = 0.0012$ s^{-1} ($\sigma_y = 264$ N mm^{-2}, $s_m = 494$ N mm^{-2}) and $\dot{e} = 140$ s^{-1} ($\sigma_y = 444$ N mm^{-2}, $s_m = 584$ N mm^{-2}), respectively. It transpires that the average values, i.e. ($W_1 + W_2$)/2 for the aluminium alloy beams and ($W_1 + W_2 + W_3 + W_4$)/4 for the mild steel beams, give good agreement with the cor-

† It appears that the inertia effects are not important in Fig. 20c because the static and dynamic curves are similar and the material is strain rate-insensitive. However, inertia could affect other parameters.
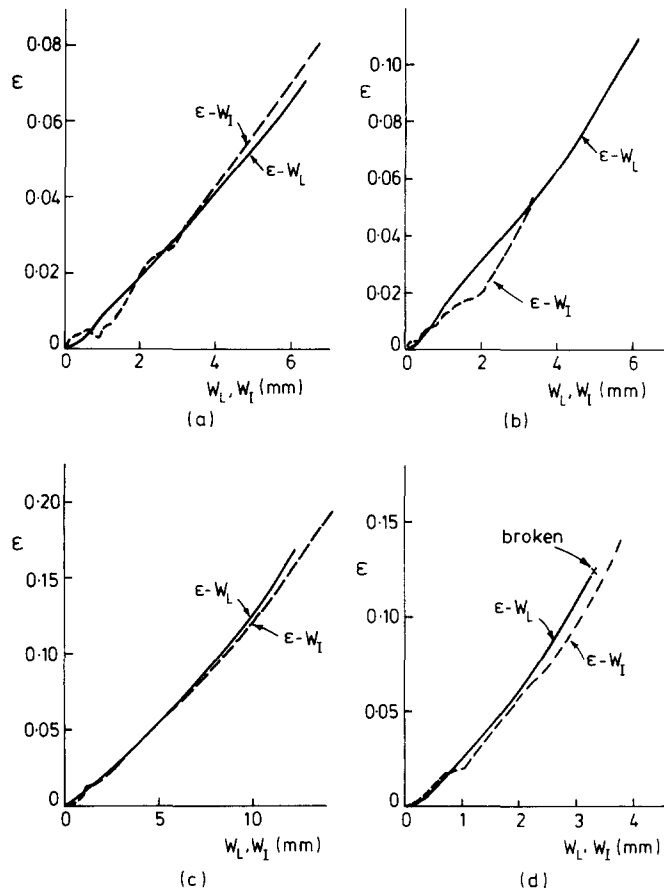
Fig. 20. Comparison of the $\varepsilon-W_L$ curves from the quasi-static tests with the $\varepsilon-W_I$ curves from the dynamic tests on beams. (a) Mild steel beams, $l_1 = 50.8$ mm. (——) SB10, quasi-static; (— — —) SB08, $V_0 = 10.6$ m s^{-1}. (b) Mild steel beams, $l_1 = 25.4$ mm. (——) SB03, quasi-static; (— — —) SB05, $V_0 = 9.2$ m s^{-1}. (c) Aluminium alloy beams, $l_1 = 50.8$ mm. (——) AB02, quasi-static; (— — —) AB05, $V_0 = 6.2$ m s^{-1}. (d) Aluminium alloy beams, $l_1 = 6.35$ mm. (——) AB03, quasi-static; (— — —) AB09, $V_0 = 3.8$ m s^{-1}.

responding experimental results. Moreoever, the deformation modes observed by a high speed camera agree with the theoretical analysis of Liu and Jones (1988). Thus, a theoretical analysis, with a simplified square yield curve for a rigid-plastic material, gives acceptable predictions from a design engineering viewpoint.

It was observed that all of the failed specimens broke at the impact point. The permanently deformed transverse profiles of the specimens which are nearly or just broken are shown in Fig. 21a–d. It is interesting to note that specimen SB07, which was impacted

Table 6. Theoretical and experimental results for the maximum permanent transverse deflection of the aluminium alloy beams

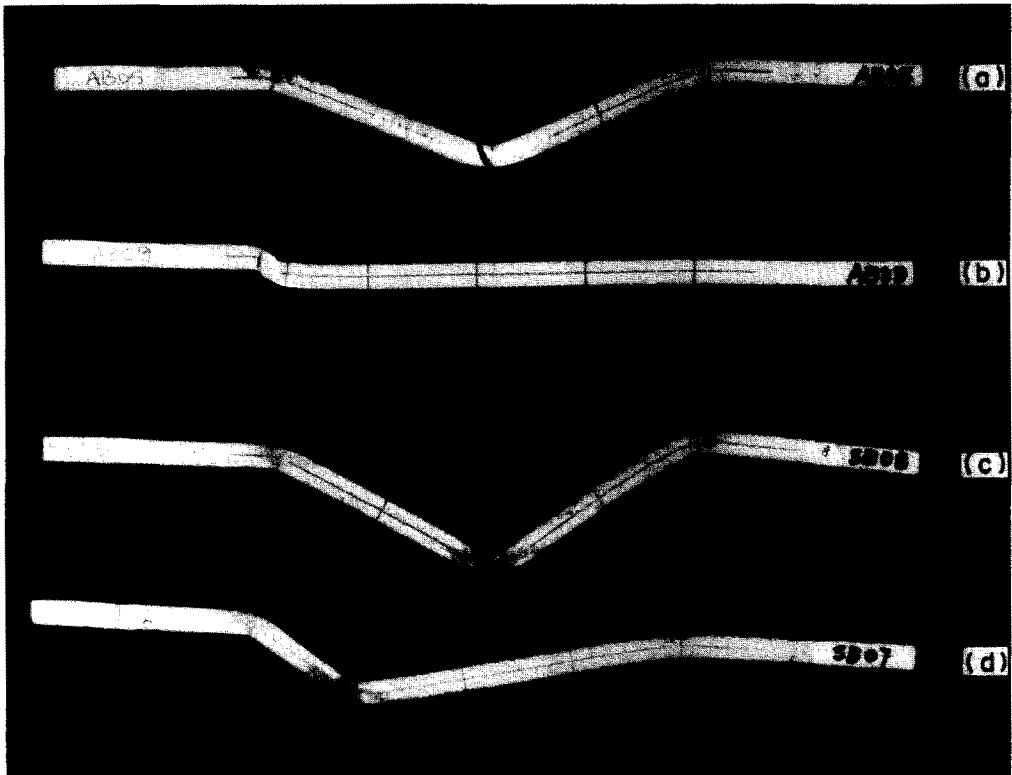| Specimen number	l_1 (mm)	V_0 (m s^{-1})	W_1 (mm)	W_2 (mm)	W_{ave}† (mm)	Experimental results		
						W_{Lp} (mm)	W_p (mm)	W_f (mm)
AB04	50.8	5.4	19.3	10.9	15.1	14.80	14.80	
AB10	50.8	5.8	20.9	11.9	16.4	15.90	15.90	
AB05	50.8	6.2	22.5	12.9	17.7			17.70
AB08	6.35	3.7	4.82	2.37	3.59	3.22	3.84	
AB09	6.35	3.8	5.02	2.48	3.75	3.60	4.18	

† $W_{ave} = (W_1 + W_2)/2$.

Fig. 21. Permanent transverse profiles of the beams after impact. (a) AB05, $l_1 = 50.8$ mm, $V_0 = 6.2$ m s^{-1}. (b) AB09, $l_1 = 6.35$ mm, $V_0 = 3.8$ m s^{-1}. (c) SB08, $l_1 = 49.9$ mm, $V_0 = 10.6$ m s^{-1}. (d) SB07, $l_1 = 25.4$ mm, $V_0 = 8.8$. m s^{-1}.
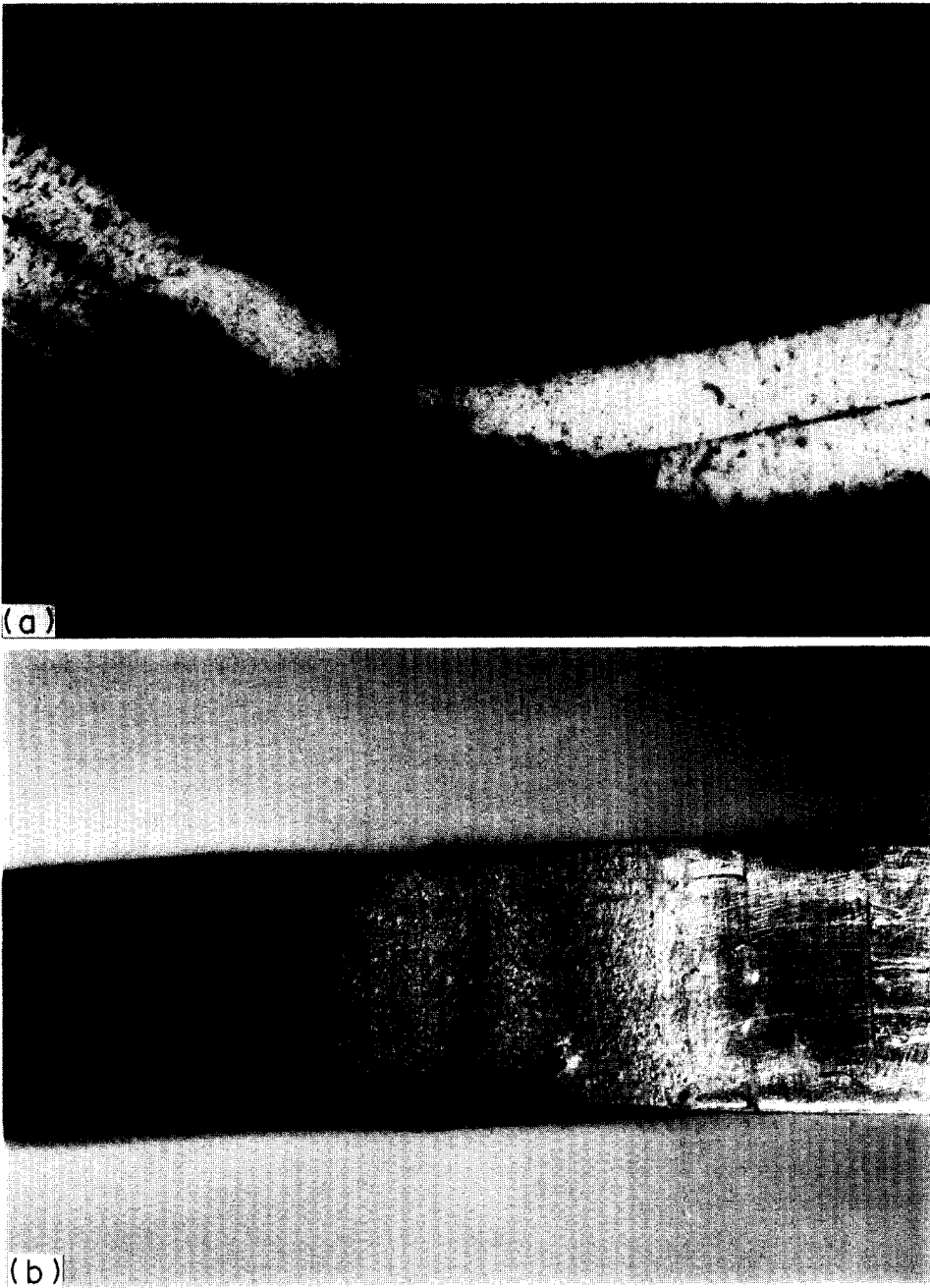
Fig. 22. Plastic deformation near the impact point of the mild steel specimen SB07 with $l_1 =$ 25.4 mm and $V_0 = 8.8$ m s^{-1}. (a) Side view of specimen showing crack at the edge of the indentation. (b) Severe plastic deformation on the lower surface.

Table 7. Theoretical and experimental results for the maximum permanent transverse deflection of the mild steel beams

Specimen number	l_1 (mm)	V_0 (m s^{-1})	W_1 (mm)	W_2 (mm)	W_3 (mm)	W_4 (mm)	W_{ave}† (mm)	W_{Lp} (mm)	W_p (mm)	W_f (mm)
								Experimental results		
SB09	50.5	10.5	25.9	18.2	19.4	16.5	20.0	20.90	20.90	
SB08	49.9	10.6	26.4	18.6	19.7	16.9	20.4			21.80
SB06	50.8	11.5	28.8	20.3	21.6	18.5	22.3			22.80
SB07	25.4	8.8	18.2	12.6	13.4	11.4	13.9	13.90	14.52	
SB05	25.4	9.2	19.2	13.3	14.2	12.0	14.7			15.0
SB04	25.4	10.1	21.0	14.6	15.6	13.3	16.1			16.0

† $W_{ave} = (W_1 + W_2 + W_3 + W_4)/4$.

at $l_1 = 25.4$ mm, cracked at the impact point and was necked severely, as shown in Fig. 22. It is evident from the locations of the crack initiation sites that the steel beams, which were struck at the mid-span or the quarter-span, failed in a shear mode, as also observed by Liu and Jones (1987a).

The failure behaviour of the aluminium alloy beams in the present test programme was somewhat different to that reported by Liu and Jones (1987a) and Jones (1989d). It was observed that flat aluminium alloy beams generally failed due to tensile tearing with a crack being initiated by the maximum tensile strain underneath the impact point on the lower surface or on the upper surface at the support for small values of l_1. The broken section of a beam with a tensile tearing failure had a zig-zag shape. However, a transverse shear failure may occur when the impact point is close to a support. In the present experimental programme, however, the broken section lay in a single plane inclined at about 45° to the beam axis, and no specimens broke at a support. Only a few tests were performed for each case so that insufficient evidence is available to verify the failure mode. Nevertheless, it is still possible to find some information on the failure mode from a careful study of the variations of the maximum permanent deflection W_p and the depth of indentation W_S with impact velocity, which are listed in Table 5.

It is evident that the axial tensile strain is related to W_p, which characterizes the overall deformation of a beam, whereas the transverse shear strain is related mostly to W_S, which is a measure of the local shear deformation. The indentations are small for the aluminium alloy beams struck at $l_1 = 50.8$ mm (specimens AB04, AB10, AB05),† but W_p increases rapidly as the impact velocity increases, indicating a tendency towards a tensile tearing failure. By way of contrast, W_p increases by 0.34 mm while W_S increases by 0.2 mm as the impact velocity, for the beams struck at $l_1 = 6.35$ mm, increases from 3.7 (specimen AB08) to 3.8 m s^{-1} (specimen AB09). This implies that during the final stage most energy is absorbed through shear deformations and failure is dominated by a shear mode.

A failure criterion in terms of the critical overall rotation angle was proposed by Yu and Jones (1989) for some aluminium alloy beams. It gave good agreement with the experimental results reported by Liu and Jones (1987a) for beams having $H = 7.62$ mm. The overall rotation angles, θ, for the current experimental test specimens are listed in Table 8. Both W_{Lp} and W_p are presented for unsymmetrical impact. The value of θ calculated from W_{Lp} is nominal, while that calculated from W_p is an overestimation since the distance from the point where W_p was measured to the nearest support is longer than l_1. It appears from Table 8 that this criterion is valid for the aluminium alloy beams but with a critical overall rotation angle $\theta_c \cong 0.65$.‡ This critical value is larger than that reported by Yu and

† The value of W_S for specimen AB05 was very small but is not reported in Table 5 because it was difficult to measure in the broken beam.

‡ This value was estimated from the results for specimen AB09 which did not fracture when $\theta = 0.63$ and specimen AB05 which broke and left a deformed shape with $\theta = 0.67$.

Table 8. Overall rotation angles calculated from experimental results

Specimen number	l_1 (mm)	V_0 (m s^{-1})	W_{Lp} (mm)	W_p (mm)	W_f (mm)	θ	Comments
SB09	50.5	10.5	20.90	20.90		0.78	
SB08	49.9	10.6			21.8	0.81	(B)†
SB06	50.8	11.5			22.8	0.84	(B)
SB07	25.4	8.8	13.90	14.52		0.68/0.71‡	(C)
SB05	25.4	9.2			15.0	0.73	(B)
SB04	25.4	10.1			16.0	0.77	(B)
AB04	50.8	5.4	14.80	14.80		0.57	
AB10	50.8	5.8	15.90	15.90		0.61	
AB05	50.8	6.2			17.7	0.67	(B)
AB08	6.35	3.7	3.22	3.84		0.50/0.58‡	
AB09	6.35	3.8	3.60	4.18		0.55/0.63‡	

† B, broken; C, cracked.
‡ Values of θ associated with W_{Lp} and W_p, respectively.

Jones (1989) for the experimental results by Liu and Jones (1987a). However, θ_c depends on the structural characteristics and material properties and in the present tests the beams are thinner and made from a different material. Further numerical studies are required to show whether or not θ_c is related to a critical tensile strain.

It transpires that a similar criterion is not evident from the mild steel beam test results reported in Table 8, which is possibly due to the influence of material strain rate sensitivity and other factors.

It is evident from Table 4 that the maximum transverse deflection at failure increases with the impact velocity for the steel beams struck at or near the mid-span. It is not known whether or not this is caused by the strain rate sensitivity of the material, although the rupture strain in Fig. 8 is essentially strain rate-insensitive. However, no experimental data were recorded for the strain distribution at the onset of fracture, which may be influenced by strain rate. Moreover, W_f is obtained using high-speed photography and is the value of W on a photograph just before a beam is broken, rather than the value of W when a crack is initiated. The relationship between the crack initiation and fracture of a beam and the influence of impact velocity have not been examined for local impact loads, although results have been reported for the shear behaviour (Jouri and Jones, 1988). It is evident that further experimental investigations and numerical simulations are required to provide further information.

4. CONCLUSIONS

Further experimental evidence is reported for the deformation and failure characteristics of clamped beams under local impact loads. The strain rate-sensitive characteristics of plastic flow and the uniaxial rupture strain were recorded up to 140 s^{-1} for the aluminium alloy and mild steel materials used in the beams. The materials data are necessary for the development of the failure criteria and the calibration of numerical programmes.

It is observed that the mild steel used in this study is less rate-sensitive at large plastic strains than at small plastic strains. The Cowper–Symonds constitutive equation fits these data with $D = 1.05 \times 10^7$ s^{-1}, $p = 8.30$ and the static uniaxial stress–strain curve shown in Fig. 5. Good agreement is found between the experimental results and this model when the axial strain is larger than 0.04. The true strain at fracture of this material is about 0.83 and is almost strain rate-insensitive. In contrast, the flow stress of the aluminium alloy is strain rate-insensitive but the true uniaxial rupture strain increases with an increase in strain rate.†
Therefore, for both materials the influence of strain rate is important in failure analyses.

† Due to the inhomogeneity of the aluminium alloy mentioned earlier, more experimental work is required to confirm this result.

Detailed information on the strain–time history, transverse displacement–time history, maximum permanent transverse deflection, indentation and failure were obtained for fully clamped aluminium alloy and mild steel beams. The beams were struck at two different positions on the span with various impact velocities. One specimen was near to the failure threshold in each type of test.

It transpires that when a beam is impacted at or near the mid-span, the indentation occurs largely during the second half of motion. It is also conjectured that the dynamic strain distribution in the mild steel beams is different from that in the corresponding quasi-static tests. This may account for some of the disagreement between the experimental results on the failure of mild steel beams and the corresponding theoretical predictions which were obtained using a strain rate-independent theory (Liu and Jones, 1987b).

This research also reveals some interesting phenomena on the rupture of beams which are not well understood. Further experimental studies as well as numerical simulations are required to achieve a better understanding. Moreover, further knowledge is required on rupture strains and on the strain rate sensitivity of materials, especially under large plastic strains. Currently, numerical simulations of the beam tests are being undertaken to obtain the rupture strains which cannot be measured using strain gauges when $\varepsilon >$ approximately 0.2.

REFERENCES

Al-Mousawi, M. M., Deans, W. F. and Reid, S. R. (1987). A new method for high rate tension test, *Int. Conf. on Impact Loading and Dynamic Behaviour of Materials*, Bremen, F.R.G.

Birch, R. S., Jones, N. and Jouri, W. S. (1988). Performance assessment of an impact rig. *Proc. Inst. Mech. Engrs* **202**(C4), 275–285.

Campbell, J. D. (1972). *Dynamic Plasticity of Metals*, Courses and Lectures No. 46 at CISM, Udine. Springer, New York.

Duffey, T. A. (1989). Dynamic rupture of shells. In *Structural Failure* (Edited by T. Wierzbicki and N. Jones), pp. 161–192. John Wiley, New York.

Harding, J. (1977). Effect of temperature and strain rate on strength and ductility of four alloy steels. *Metals Technol.* 6–16.

Johnson, W. (1972). *Impact Strength of Materials*. Edward Arnold, London and Crane Russak, New York.

Jones, N. (1976). Plastic failure of ductile beams loaded dynamically. *Trans. ASME, J. Engng Ind.* **98B**, 131–136.

Jones, N. (1989a). Recent progress in the dynamic plastic behaviour of structures, Part 5. *Shock Vibr. Digest* **21**(8), 3–13.

Jones, N. (1989b). Recent studies on the dynamic plastic behaviour of structures. *Appl. Mech. Rev.* **42**(4), 95–115.

Jones, N. (1989c). *Structural Impact*. Cambridge University Press, Cambridge, U.K.

Jones, N. (1989d). On the dynamic inelastic failure of beams. In *Structural Failure* (Edited by T. Wierzbicki and N. Jones), pp. 133–159. John Wiley, New York.

Jones, N. (1989e). Some comments on structural impact. In *Supercomputing in Engineering Structures* (Edited by P. Melli and C. A. Brebbia), pp. 133–157. Computational Mechanics Publications, Southampton and Boston, co-published with Springer, New York.

Jones, N. (1989f). Some comments on the modelling of material properties for dynamic structural plasticity. In *Fourth Int. Conf. on the Mechanical Properties of Materials at High Rates of Strain*, Oxford (Edited by J. Harding), pp. 435–445. Institute of Physics Conf. Series No. 102.

Jouri, W. S. and Jones, N. (1988). The impact behaviour of aluminium alloy and mild steel double-shear specimens. *Int. J. Mech. Sci.* **30**(3/4), 153–172.

Kawata, K., Fukui, S., Seino, J. and Takada, W. (1968). Some analytical and experimental investigations on high velocity elongation of sheet materials by tensile shock. *IUTAM, Behaviour of Dense Media under High Dynamic Pressure*, Paris, Dunod, pp. 313–323.

Liu, J. H. and Jones, N. (1987a). Experimental investigation of clamped beams struck transversely by a mass. *Int. J. Impact Engng* **6**(4), 303–335.

Liu, J. H. and Jones, N. (1987b). Plastic failure of a clamped beam struck transversely by a mass, University of Liverpool, Department of Mechanical Engineering Report ES/31/87, presented at A. Sawczuk Memorial Symp., Rytro, Poland. To be published by Pineridge Press, Swansea.

Liu, J. H. and Jones, N. (1988). Dynamic response of a rigid plastic clamped beam struck by a mass at any point on the span. *Int. J. Solids Structures* **24**(3), 251–270.

Menkes, S. B. and Opat, H. J. (1973). Broken beams. *Exp. Mech.* **13**, 480–486.

Metals Handbook (1985). 9th Edn, Vol. 8. ASM.

Reid, S. R. (1985). *Metal Forming and Impact Mechanics*. Pergamon Press, Oxford.
Soroushian, P. and Choi, K. B. (1987). Steel mechanical properties at different strain rates. *Proc. ASCE, J. Struct. Engng* **113**(4), 663–672.
Symonds, P. S. (1965). Viscoplastic behaviour in response of structures to dynamic loading. *Behaviour of Materials Under Dynamic Loading* (Edited by N. J. Huffington), pp. 106–124. ASME, New York.
Symonds, P. S. (1967). Survey of methods of analysis for plastic deformation of structures under dynamic loading, Brown Univ., Div. of Engng, Report BU/NSRDC/1-67.
Yu, J. L. and Jones, N. (1989). Numerical simulation of a clamped beam under impact loading. *Comput. Struct.* **32**(2), 281–293.

APPENDIX A

During a tensile test, plastic flow occurs within a length of a specimen which can be estimated from the dimensions of the specimen with little error provided that this section is sufficiently long so that the influence of the two enlarged ends is negligible. If this length is taken as the gauge length for engineering strain, an entire engineering stress–strain curve can be obtained from the records of cross-head displacement and load for quasi-static and dynamic tests.

In comparison with the time duration of a test, the time for an elastic wave to propagate through the machine is very short. Thus, the influence of inertia on the measuring system is negligible, except in the initial stage of the tests at the highest strain rates ($\dot{e} = 140 \text{ s}^{-1}$), when the influence of inertia on the stress distribution within the specimen is significant and the results in the initial phase are not acceptable (see footnote ‡ in Section 2.2). Thus, with the above exception, the whole system from the base of the test machine to the cross-head member may be simplified as a structure consisting of two parts. One is a section of length L_0 within which plastic flow is confined during a test, and the other is an equivalent length L_1, which deforms linear-elastically, as shown in Fig. A1. Thus,

$$s = P/A_0 \quad \text{and} \quad e = \Delta L_0/L_0. \tag{A1a,b}$$

The total cross-head displacement is equal to $\Delta L_0 + \Delta L_1$, where before yielding, the specimen is elastic, and

$$\Delta L_0 = L_0 P/A_0 E, \tag{A2}$$

so that ΔL_1 may be obtained by subtracting eqn (A2) from the cross-head displacement records. Therefore, the variation of ΔL_1 with load after yielding is obtained by linear extrapolation.

Now, a stress–apparent strain curve may be drawn in the (s, e) plane as shown in Fig. A2 when using the
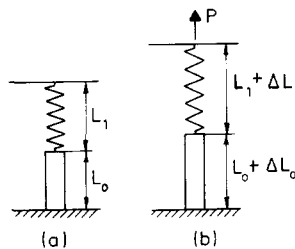

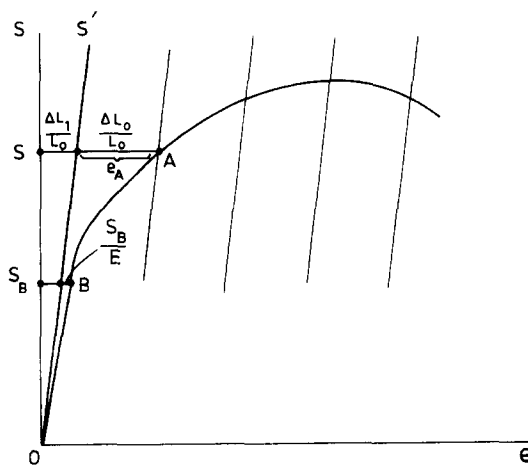Fig. A1. Simplified tensile test system. (a) Before loading. (b) After loading.

Fig. A2. Method of obtaining the engineering stress–strain curve from the apparent curve based on the cross-head displacement and load cell records.

cross-head displacement for the extension of a specimen. The actual elastic strain is then calculated for a typical point B on the elastic part of this curve to give the contribution of ΔL_1 to the apparent strain at this point. Thus, for an arbitrary point on the apparent curve in Fig. A2, say point A, the apparent strain is divided by the axis os' into two parts,

$$e' = \Delta L_1/L_0 \quad \text{and} \quad e = \Delta L_0/L_0, \tag{A3a,b}$$

where e is the actual engineering strain. In other words, the actual engineering stress–strain relation can be read from the $s'\!-\!e$ coordinate system in Fig. A2.

APPENDIX B

From eqn (3) we have

$$\log{(\sigma/\sigma_0(\varepsilon) - 1)} = (1/p)(\log \dot{\varepsilon} - \log D). \tag{B1}$$

Using this expression, a least square fit is first made for true stresses at a specified value of true strain with a different choice of static stress $\sigma_0(\varepsilon)$. A value of $\sigma_0(\varepsilon)$ is then found which gives the best fit, as indicated by the largest correlation coefficient. This is repeated for seven different values of ε ($\varepsilon = 0.03, 0.05, 0.10, 0.15, 0.20$ and 0.25 before necking and $\varepsilon = 0.80$ near fracture with a straight line for $\varepsilon \geq 0.25$) to establish a fictitious static stress–strain curve. However, the values p and D so obtained are somewhat different for each value of ε. Hence the final values of $1/p$ and $\log D$ are average values associated with four typical values of true strain, i.e. $\varepsilon = 0.05, 0.10, 0.15$ and 0.80.